Materials & Design 232 (2023) 112141

Contents lists available at ScienceDirect

Materials & Design

journal homepage: www.elsevier.com/locate/matdes

Achieving ultrahigh strength in oxide-dispersion-strengthened CoCrNi alloy via in situ formation of coherent Y-Ti-O nanoprecipitates

Wenhao Mao [a,1], Lu Yang [a,1], Feilong Jiang [a], Jiangping He [a], Junhua Luan [b], Zengbao Jiao [c], Fuzeng Ren [a,*]

[a] Department of Materials Science and Engineering, Southern University of Science and Technology, Shenzhen, Guangdong 518055, China
[b] Department of Materials Science and Engineering, City University of Hong Kong, Hong Kong, China
[c] Department of Mechanical Engineering, The Hong Kong Polytechnic University, Hong Kong, China

ARTICLE INFO

Keywords:
CoCrNi
Medium-entropy alloy
Oxide dispersion strengthening
Coherent nanoprecipitates

ABSTRACT

Oxide-dispersion-strengthened CoCrNi alloys were fabricated via in situ oxidation by adding Ti and Y, and non-in-situ oxidation by direct addition of Ti and Y_2O_3, referring to as Y-ODS and Y_2O_3-ODS alloys, respectively. Transmission electron microscopy (TEM) and atom probe tomography (APT) characterizations reveal that both alloys consist of an ultrafine-grained face-centered-cubic (fcc) matrix, a high number density of nanoscale Y-Ti-O precipitates and a small number of $(Cr_{0.75}Ti_{0.25})_2O_3$ oxides. However, the nanoscale Y-Ti-O precipitates in the two alloys show distinct phase and microstructure. The Y_2O_3-ODS alloy contains only incoherent orthorhombic Y_2TiO_5 nanoprecipitates, but the Y-ODS alloy also contains a high density of fully coherent pyrochlore $Y_2Ti_2O_7$ nanoprecipitates. The Y-ODS alloy achieves an ultrahigh yield strength of 1660 MPa, which is 320 MPa higher than that of the Y_2O_3-ODS one, but maintains the same ductility. Quantitative analysis of the strengthening mechanism indicates that such large difference in strength is mainly attributed to the presence of coherent $Y_2Ti_2O_7$ nanoprecipitates in Y-ODS alloy. This study should provide significant insight into the design of ODS high/medium-entropy alloys via in situ oxidation during mechanical alloying and consolidation.

1. Introduction

CoCrNi medium-entropy alloy (MEA) has a single-phase, face-centered-cubic (fcc) crystal structure and demonstrated excellent ductility and exceptional damage-tolerance at cryogenic temperatures [1,2], due to its low stacking fault energy which promotes the formation of deformation twins [3]. Twinning introduces extra twin boundaries that can impede dislocation motion and hence promotes a high work hardening rate, which in turn allows the onset of necking to be postponed and thus increases ductility. In addition, deformation-induced phase transformation from the fcc matrix to the hexagonal close-packed (hcp) phase may also contribute its plasticity [4] and cryogenic toughness [5]. However, single-phase coarse-grained CoCrNi usually shows low yield strength (below 400 MPa) at ambient temperature and elevated temperature [6,7]. Consequently, various processing methods were developed to strengthen CoCrNi, including grain boundary strengthening via severe plastic deformation [8,9], solid solution strengthening via addition of alloying elements [10,11], and precipitation strengthening via the formation of heterogeneous $L1_2$-type precipitates [6,12,13]. These processing methods have significantly enhanced the strength of CoCrNi MEA and simultaneously maintain considerable ductility. However, such strengthening mechanisms may become ineffective at high temperature or upon exposure to irradiation damage due to grain coarsening or dissolution of precipitates, resulting in apparent decrease in mechanical properties [14].

Oxide dispersion strengthening (ODS) is an effective strengthening mechanism where the nanoscale dispersoids act as barriers against dislocation motion and grain growth [14,15]. Nanostructured ODS alloys possess remarkable high-temperature strength, chemical and structural stability, and extraordinary resistance to creep and irradiation damage, and hence have been developed as promising candidates for use in extremely harsh environments [16–18]. The most representative case is steels strengthened by the addition of Y_2O_3 and Ti, where Ti is used to refine the dispersion through the precipitation of nanoscale Y-Ti-O particles. These ODS steels have a unique microstructure of a high number density of Y-Ti-O nanoparticles uniformly dispersed in the

* Corresponding author.
E-mail address: renfz@sustech.edu.cn (F. Ren).
[1] These authors contributed equally to this work.

https://doi.org/10.1016/j.matdes.2023.112141
Received 13 February 2023; Received in revised form 2 July 2023; Accepted 4 July 2023
Available online 7 July 2023

ferritic or austenitic matrix [19–21]. The Y-Ti-O nanoparticles act as fixed pinning points for dislocation motion and as a sink of point defects induced by radiation displacement, which contribute to excellent mechanical properties and irradiation tolerance [22,23]. Therefore, ODS might be a promising approach to strengthen CoCrNi MEA but this remains lack of in-depth investigation.

In ODS alloys, Y-Ti-O nanoparticles are generally considered as the key component for enhancing mechanical properties. The mechanical properties and microstructure stability of alloys are greatly affected by the structure, size, distribution, and composition of the nanoparticles. According to transmission electron microscopy (TEM) observations [24–26], the Y-Ti-O nanoparticles are mainly assigned to two equilibrium phases, $Y_2Ti_2O_7$ and Y_2TiO_5. Density functional theory-based calculations also predict that the formation enthalpies of $Y_2Ti_2O_7$ and Y_2TiO_5 are more negative and hence their formation is favored over other likely oxides [27]. Interestingly, Unifantowicz et al. [28] identified a new type of nanoparticle, $YTiO_3$ oxide with orthorhombic lattice, in ODS reduced activation ferritic steels. Recently, Spartacus et al. [29] revealed the chemical and structural evolution of the nano-oxides throughout the consolidation process of ODS ferritic steels using multi-technique characterization. In addition, the orientation relationship and coherency between the nanoprecipitates and the matrix are also closely related to mechanical properties of materials. Hirata et al. [30] found that the small Y-Ti-O nanoclusters with a defective NaCl structure (< 5 nm) had a high lattice coherency with the body-centered-cubic (bcc) ferrite matrix. Ribis et al. [31] revealed that the $Y_2Ti_2O_7$ nanoparticles were coherent and had a cube-on-cube orientation relationship with the ferritic matrix. However, up to now, there has been no report on the interface orientation relationship between the Y-Ti-O nanoprecipitates and the fcc CoCrNi MEA matrix, and the strengthening mechanism is yet to be unraveled.

In this work, oxide-dispersion-strengthened ultrafine-grained CoCrNi MEAs were fabricated by mechanical alloying and spark plasma sintering (SPS). Two distinct powder blending procedures were proposed to fabricate the alloys of interest, as illustrated in Fig. 1: (1) direct addition of Y_2O_3 powder to the Co, Cr, and Ni powder mixture; and (2) introducing pure metallic Y powder (with the equivalent amount of Y to that in the Y_2O_3 powder) to form oxides in situ, because Y is a chemically reactive element which has high affinity to O. The corresponding two alloys are referred to as Y_2O_3-ODS and Y-ODS CoCrNi alloys, respectively. Then, a comparative study on their microstructure and mechanical properties was performed. Atom probe tomography (APT) was used to analyze the composition of the matrix and nanoprecipitates in the Y-ODS alloy. Finally, the strengthening mechanism of the Y-ODS CoCrNi alloy was revealed. This study should provide significant insight into the design of ODS high/medium-entropy alloys and advance the understanding of their strengthening mechanisms.

2. Experimental procedures

2.1. Alloy fabrication

Mechanical alloying is a prerequisite processing for ODS alloys, which would not only promote the uniform distribution of the oxides in the matrix, but also refine the particle size and grain size [14]. SPS has the advantage of fast heating rate, low sintering temperature, and short sintering time which can achieve high density and avoid grain coarsening. Thus, a combination of mechanical alloying and SPS was used to fabricate the present ODS alloys. The fabrication procedure of both ODS CoCrNi alloys were schematically illustrated in Fig. 1. Specifically, initial elemental powders (purity ≥ 99.2 wt%, size ≤ 300 mesh) of Co, Cr, and Ni were first mixed with an equiatomic ratio. For Y_2O_3-ODS CoCrNi alloy, 0.25 wt% Y_2O_3 powder (purity ≥ 99.9 wt%, size ≤ 50 nm) and 0.4 wt% Ti powder (purity ≥ 99.5 wt%, size ≤ 325 mesh) were directly added to the equiatomic Co, Cr and Ni powder mixture, while for Y-ODS CoCrNi alloy, instead of using Y_2O_3, 0.2 wt% Y powder (purity ≥ 99.9 wt%, size ≤ 325 mesh) and 0.4 wt% Ti powder were added to the Co, Cr and Ni powder mixture, where the atomic percentage of Y in these two alloys was maintained the same. Both groups of powder mixtures were sealed in hardened steel vials with hardened steel balls (ball-to-powder weight ratio of 5:1) and subjected to high-energy ball milling using a SPEX 8000D mixer (SPEX SamplePrep LLC, Metuchen, New Jersey, USA) at ambient temperature in an argon-filled glove box (oxygen content: ~10 ppm) for 15 h. Subsequently, the 15 h-milled powders were compacted into bulk by SPS (SPS-211Lx, Fujidempa Kogyo. Co., Ltd., Osaka, Japan) at 1100 °C and 60 MPa for 15 min in a vacuum environment of ~6 Pa. The relative density of the sintered bulk alloys exceeded 99%, measured using Archimedes method.

2.2. Microstructure characterization

The phases of both the ball-milled powders and as-compacted bulk alloys were identified by X-ray diffraction (XRD; Smartlab-9 kW, Rigaku, Japan) in a 2θ range from 20° to 100° using a Cu-Kα radiation (λ =

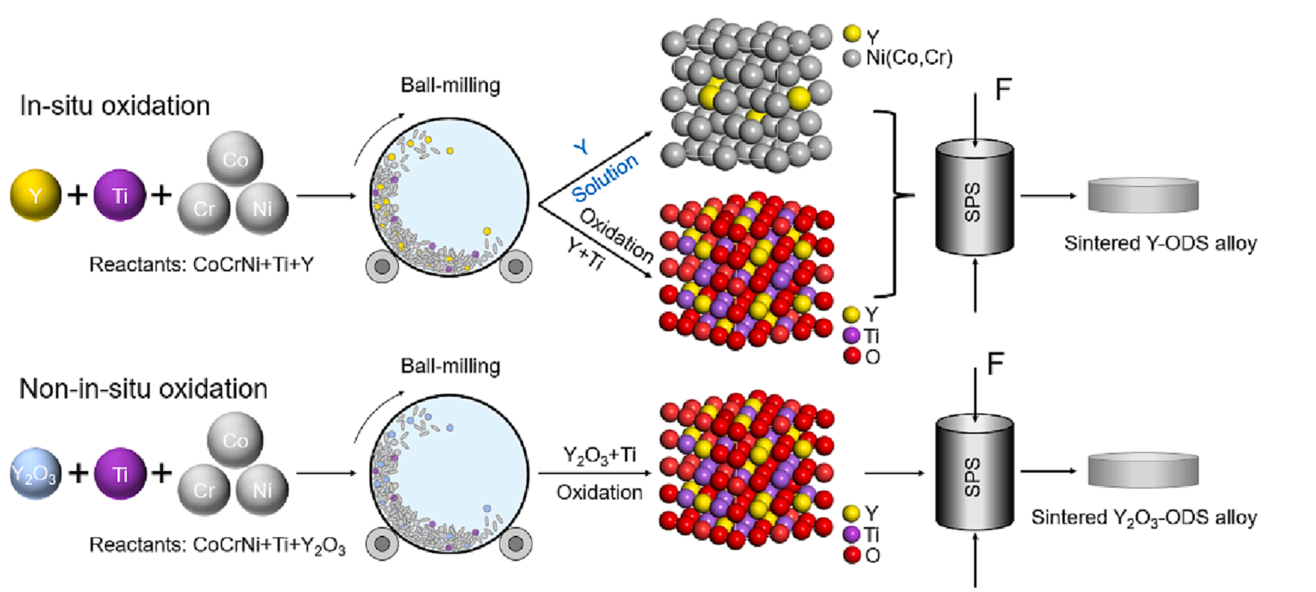

Fig. 1. Schematic of the fabrication of Y-ODS and Y_2O_3-ODS CoCrNi alloys.

0.154 nm, 45 kV, 200 mA) with a step size of 0.01° and a scanning speed of 10° min^{-1}. The morphology and grain size of the as-fabricated alloys were examined by scanning electron microscopy (SEM; TESCAN MIRA 3, Czech Republic) equipped with electron backscattered diffraction (EBSD; Nordlys Max2, Oxford Instruments plc, Oxford, UK) detector. Transmission electron microscopy (TEM), selected area electron diffraction (SAED), high-resolution TEM, and high-angle annular dark-field scanning TEM (HAADF-STEM) were performed on an FEI Tecnai F30 TEM equipped with energy-dispersive X-ray spectroscopy (EDX) detector operated at 300 kV (FEI Technologies Inc, Hillsboro, Oregon, USA) to characterize the microstructure in detail. All the TEM samples were prepared by focused ion beam (FIB; Helios Nanolab™ 600i, FEI Technologies Inc, Oregon, USA) site-specific standard lift-out technique.

The three-dimensional (3D) elemental distribution was studied using APT. This was accomplished by a local electrode atom probe (CAMEACA LEAP 5000 XR) analyzed at 70 K in voltage mode, with a pulse repetition rate of 200 KHz, a pulse fraction of 20% and an evaporation detection rate of 0.15% atom per pulse. The 3D atom distribution was visualized using Integrated Visualization and Analysis Software (IVAS) version 3.8 software. The needle-shaped specimen of APT was prepared by lift-out and annular-milled in a FEI Scios FIB/SEM. The average grain size and volume fraction of oxides and nanoprecipitates were measured by statistical image analysis using Image-pro-plus 6.0 software.

2.3. Mechanical testing

Tensile tests were conducted at ambient temperature with a strain rate of 5×10^{-4} s^{-1}, using a universal testing machine (CMT5105, MTS, China). The dog-bone-shaped tensile specimens with a gauge dimension of 4 mm × 2 mm × 1 mm were machined using electrical discharge machining. The test section of the specimens was painted with a fine and diffuse black speckle pattern on a white undercoat to identify the deformation using the 2D stereo digital image correlation (DIC) method. Three independent tests were performed for each alloy to confirm the reproducibility.

3. Results

3.1. Phase and microstructure of the ODS CoCrNi alloys

Fig. 2 shows the XRD patterns of the initial powder mixture and the powders after ball milling for the fabrication of Y-ODS CoCrNi alloy with varying times. The XRD pattern of the initial powder mixture (Fig. 2a) shows the presence of Co, Cr, and Ni. The reflections of Ti and Y are almost invisible due to their small contents. With the increase of ball milling time, the diffraction peaks of Co and Cr gradually disappeared (Fig. 2b). After 15 h of ball milling, only the reflections of the fcc phase were detected, which suggests that Co and Cr had completely dissolved into Ni and a solid solution with fcc structure was formed due to the severe plastic deformation induced by ball milling. There was no 2θ shift in the diffraction peak position upon further extending the ball milling time from 15 h to 18 h, but with peak broadening and intensity reduction, suggesting reduced grain size and larger residual strain in the fcc solid solution. Similar behaviors also occurred in the Y_2O_3-ODS CoCrNi alloy (Supplementary Fig. S1).

Fig. 3 shows the microstructure of the powder after 15 h of ball milling for the Y-ODS CoCrNi system. The nanoscale grains show nearly equiaxed morphology, and statistical analysis shows that the ball-milled powder has an average grain size of 32 nm (Fig. 3a). A high density of dislocations or stacking faults were located in almost every grain due to severe plastic deformation induced by mechanical alloying (Fig. 3b). HAADF-STEM image and corresponding EDX elemental maps (Fig. 3c-i) reveal that the nanometric clusters are rich in Y, Ti and O. Such nanoclusters are almost uniformly dispersed in the matrix. In addition to forming oxides, partial oxygen was dissolved into the matrix (Fig. 3e). EDX quantitative analysis shows that the atomic ratios of O, Y, Ti, Co, Cr and Ni are 1.44%, 0.14%, 0.41%, 31.81%, 29.94% and 33.42%, respectively. However, it should be noted that the relative content of O may not be very accurate because EDX is insensitive to detect light elements and the measured region is rather local. Besides, 2.83 at.% Fe contamination was also detected, which should be from the milling media (hardened steel vials and balls) (Fig. 3j).

Fig. 4a shows a comparison of the XRD patterns of the spark-plasma-sintered (SPSed) Y-ODS and Y_2O_3-ODS CoCrNi alloys. Only fcc phase as that of the CoCrNi MEA was detected in both XRD patterns. It is noted that the diffraction peaks of Y-ODS alloy slightly shift to smaller 2θ angles compared with Y_2O_3-ODS alloy, indicating the increase of lattice parameter. SEM image (Fig. 4b) of the Y-ODS alloy confirms the high relative density of the bulk alloy and no pores were found on the polished sample surface. Besides, the tiny black oxide particles (as marked by white circles in Fig. 4b) has a uniform distribution in the matrix. EBSD band contrast map (Fig. 4c) shows the presence of nanoscale twins due to low stacking fault energy of CoCrNi MEA. EBSD inverse pole figure (IPF) map (Fig. 4d) reveals the heterogeneous grain structure of the fcc matrix, with the grain size ranging from 100 nm to 1200 nm with an average of 282 nm (Fig. 4e). Kernel average misorientation (KAM) map (Fig. 4f) indicates some local residual stress present in the sintered bulk alloy.

The HAADF-STEM image of Y-ODS alloy (Fig. 5a) shows two contrasts. Corresponding bright-field TEM image (Fig. 5b) reveals that the dark oxides are mainly located at the grain boundaries. High-resolution TEM analysis confirms the fcc structure of the CoCrNi matrix (Fig. 5c). SAED pattern (Fig. 5d) and high-resolution TEM image (Fig. 5e) further confirms the presence of twins inside the fcc matrix. The SAED pattern shows that the dark particle has hcp structure, analogous to that of Cr_2O_3 (Fig. 5f). A HAADF-STEM image and corresponding EDX elemental maps show that the dark particles are rich in O, Ti, and Cr (Fig. 5g). The fcc matrix has a uniform distribution of the constituent elements Co, Cr, and Ni. Quantitative EDX analysis reveals that the fcc matrix contains 29.88 at.% Co, 27.86 at.% Cr, 29.48 at.% Ni, while the

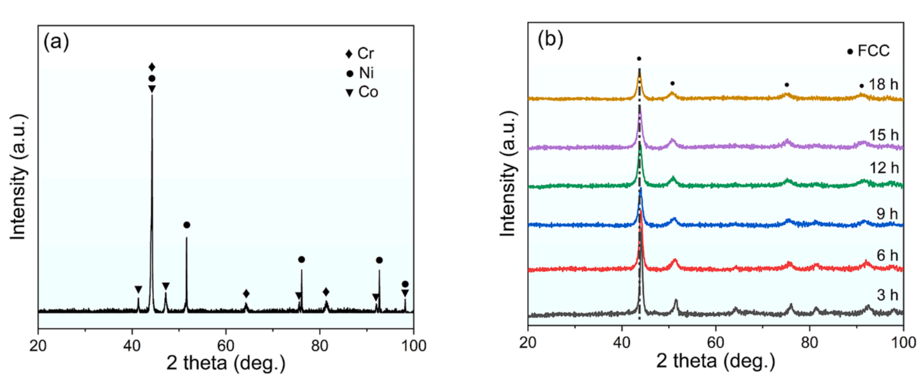

Fig. 2. XRD patterns of (a) the initial powder mixture and (b) the powders after ball milling for different times for the fabrication of Y-ODS CoCrNi alloy.

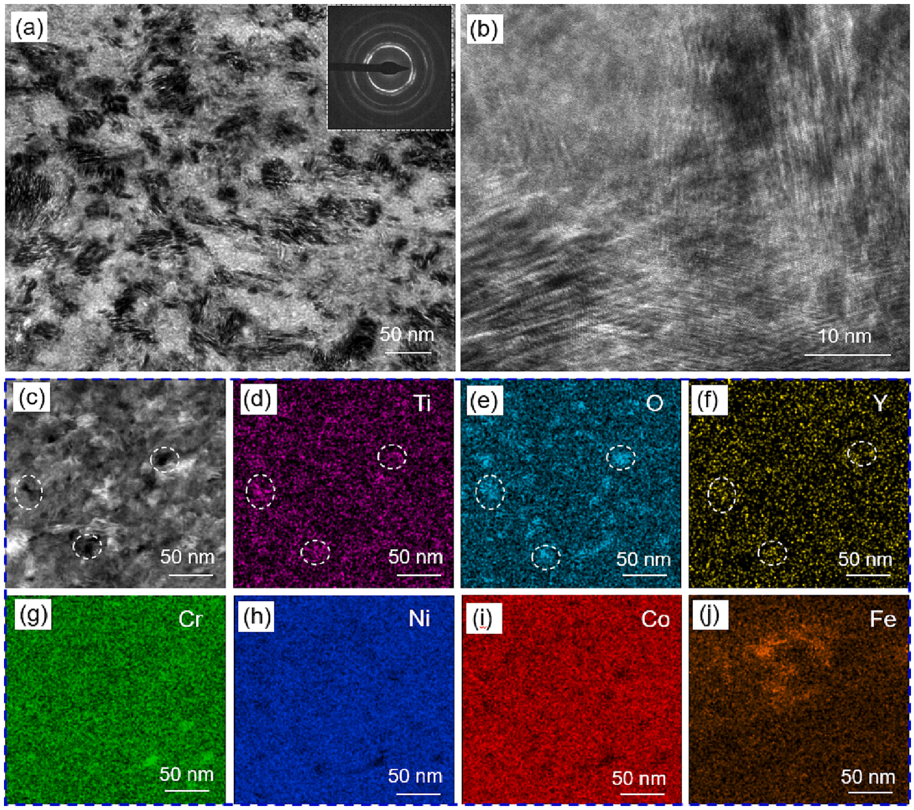

Fig. 3. Microstructure of the powder after 15 h of ball milling for the Y-ODS CoCrNi system. (a) Bright-field TEM image and corresponding SAED pattern (inset); (b) high-resolution TEM image; (c-j) HAADF-STEM image and corresponding EDX elemental maps.

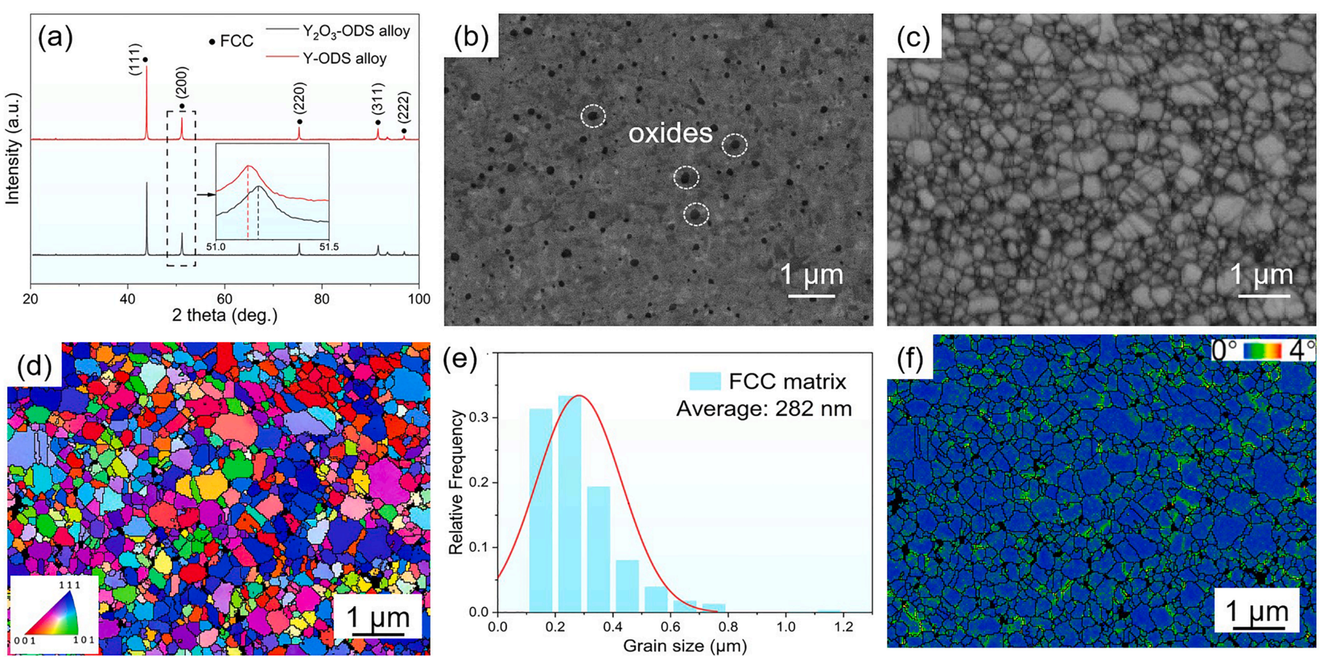

Fig. 4. Phase and microstructure of the bulk Y-ODS CoCrNi alloy. (a) XRD patterns; (b) SEM image; (c) EBSD band contrast map; (d) EBSD IPF map; (e) grain size distribution of the fcc matrix; and (f) EBSD KAM map.

dark particles contains 61.72 at.% O, 27.62 at.% Cr, 9.28 at.% Ti, and a trace amount of Co, Ni, and Y. Therefore, the dark oxide particles with hcp structure could be assigned to be $(Cr_{0.75}Ti_{0.25})_2O_3$. High-resolution TEM image along with a fast Fourier transform (FFT) pattern of the oxide (Fig. 5h) further confirms the hcp structure of the $(Cr_{0.75}Ti_{0.25})_2O_3$ oxide particles.

A high-magnification HAADF-STEM image of Y-ODS alloy (Fig. 6a) clearly shows a high number density of spherical nanoprecipitates. Statistical analysis shows that the size of the nanoprecipitates follows a normal distribution with an average of 11 nm (Fig. 6b). A higher

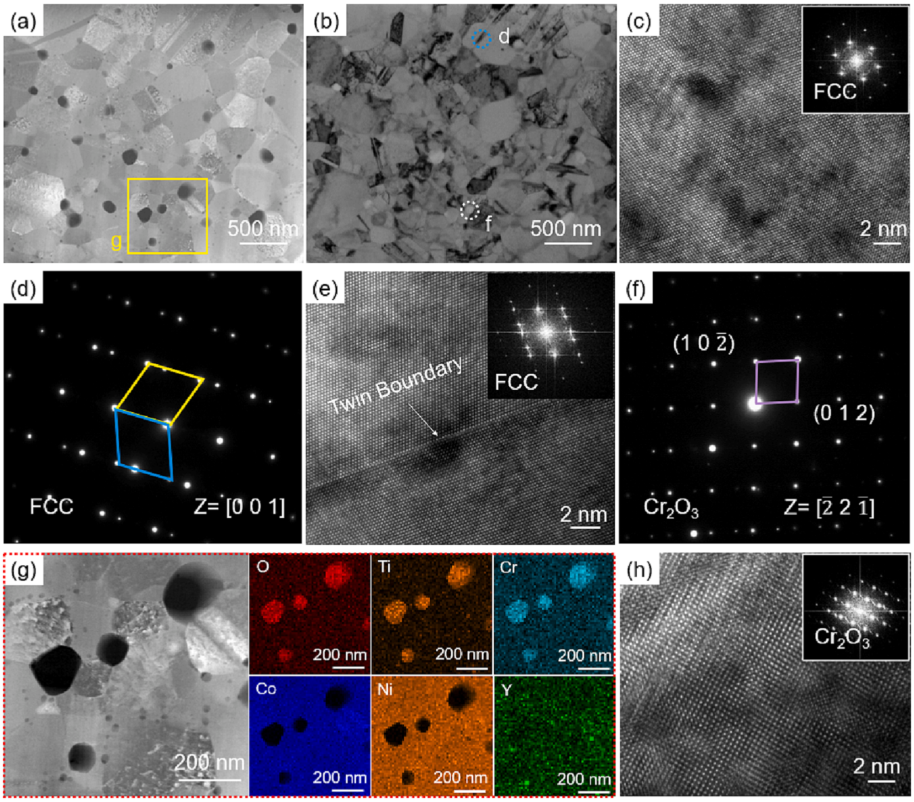

Fig. 5. Microstructure of the bulk Y-ODS CoCrNi alloy. (a) HAADF-STEM image; (b) corresponding bright-field TEM image of (a); (c) high-resolution TEM image of the fcc matrix grain with an FFT pattern (inset); (d) SAED pattern of the twin in (b); (e) high-resolution TEM image of the fcc matrix grain showing twin boundary along with an FFT pattern (inset); (f) SAED pattern of the oxides in (b); (g) enlarged HAADF-STEM image from yellow square in (a) and corresponding STEM-EDX elemental maps; and (h) high-resolution TEM image of a representative oxide grain with an FFT pattern (inset). (For interpretation of the references to colour in this figure legend, the reader is referred to the web version of this article.)

magnification HAADF-STEM shows a typical spherical nanoprecipitate (Fig. 6c). EDX line profiles across the nanoprecipitate reveal that the nanoprecipitate is rich in Ti and Y but depleted in Co, Cr, and Ni (Fig. 6d). EDX elemental maps (Fig. 6e) also suggest that the nanoprecipitates are rich in Ti and Y. High-resolution TEM analysis reveals that the nanoprecipitates have two types of crystal structure, the fully coherent $Y_2Ti_2O_7$ pyrochlore structure (Fig. 6f) and the incoherent Y_2TiO_5 orthorhombic structure (Fig. 6g) with the fcc matrix.

To show the difference between in-situ oxidation and non-in-situ oxidation in CoCrNi MEA, the microstructure of bulk Y_2O_3-ODS CoCrNi alloy was also characterized (Fig. 7). Similar to Y-ODS CoCrNi alloy, the Y_2O_3-ODS CoCrNi alloy also contains three phases, namely fcc matrix, $(Cr_{0.75}Ti_{0.25})_2O_3$ oxides, and Y-Ti-O nanoprecipitates, with an average size of 385 nm (Fig. 7c), 97 nm (Fig. 7g), and 17 nm (Fig. 7j), respectively. Compared with Y-ODS alloy, the Y_2O_3-ODS CoCrNi alloy shows slightly larger sizes of the fcc matrix grains and the nanoprecipitates but a similar size of $(Cr_{0.75}Ti_{0.25})_2O_3$ oxides. Interestingly, only orthorhombic Y_2TiO_5 structure was detected in Y_2O_3-ODS alloy (Fig. 7h-i). The lattice misfit ε^* between the Y_2TiO_5 nanoprecipitate and the matrix was calculated to be 0.43 based on $d_1 = d\{1\,1\,0\}_{matrix} = 2.438$ Å and $d_2 = d\{1\,3\,0\}_{Y2TiO5} = 3.774$ Å. The large misfit value suggests that the Y_2TiO_5 nanoprecipitates are incoherent [31]. No $Y_2Ti_2O_7$ pyrochlore structure coherent with fcc matrix was found, which is different from the Y-ODS alloy.

3.2. Mechanical property

Fig. 8a shows the tensile engineering stress–strain curves of the Y-ODS and Y_2O_3-ODS CoCrNi alloys. Interestingly, the Y-ODS CoCrNi alloy shows ~24% higher in yield strength of up to 1660 MPa while maintains the same elongation. This means that Y-ODS CoCrNi alloy formed by in-situ oxidation can reach an extremely high yield strength without loss of the ductility in comparison with the Y_2O_3-ODS alloy synthesized via non-in-situ oxidation. The presence of fully coherent pyrochlore $Y_2Ti_2O_7$ nanoprecipitates in the Y-ODS alloy is beneficial to delay the nucleation and propagation of cracks during tensile deformation, resulting in the same elongation but higher strength. A comparison of tensile yield strength/elongation to failure with other works [11,19,32–45] indicates that the Y-ODS alloy has an outstanding yield strength (Fig. 8b). To reveal the ODS effect, the SPSed CoCrNi MEA was prepared using the same processing parameters. Its microstructure was described in detail in our previous work [46]. Compared with the SPSed CoCrNi MEA, the Y_2O_3-ODS and Y-ODS alloys show 41% and 75% increase in yield strength, respectively, which indicates that both strategies show strong oxide dispersion strengthening effect.

4. Discussion

4.1. Strengthening mechanisms

The above results have demonstrated that the Y-ODS CoCrNi alloy via in situ oxidation leads to significant enhancement in strength but without compromising the ductility compared with the Y_2O_3-ODS one via non-in-situ oxidation. Therefore, it is necessary to investigate the strengthening contribution to the high yield strength at gigapascal level of the two sintered samples and discuss the reason for higher strength of Y-ODS alloy. For SPSed ODS alloys, the yield strength is believed to originate from the intrinsic frictional stress of the CoCrNi matrix(σ_0 = 218 MPa [47]), solid solution strengthening caused by adding larger atoms Ti (r_{Ti} = 1.47 Å) and Y (r_Y = 1.8 Å) ($\Delta\sigma_{SS}$), grain boundary strengthening following the Hall-Petch relationship [48] ($\Delta\sigma_{GB}$), twin boundary strengthening from the strengthening effect of twin boundaries ($\Delta\sigma_{TB}$), dispersed $(Cr_{0.75}Ti_{0.25})_2O_3$ oxide particles strengthening ($\Delta\sigma_O$), precipitation strengthening from the high number density of nanoprecipitates ($\Delta\sigma_P$), and dislocation strengthening from the interplay of pre-existing dislocations ($\Delta\sigma_{Dis}$). Hence, the overall yield strength (σ_Y) can be expressed as:

$$\Delta\sigma_Y = \Delta\sigma_0 + \Delta\sigma_{SS} + \Delta\sigma_{GB} + \Delta\sigma_{TB} + \Delta\sigma_O + \Delta\sigma_P + \Delta\sigma_{Dis} \quad (1)$$

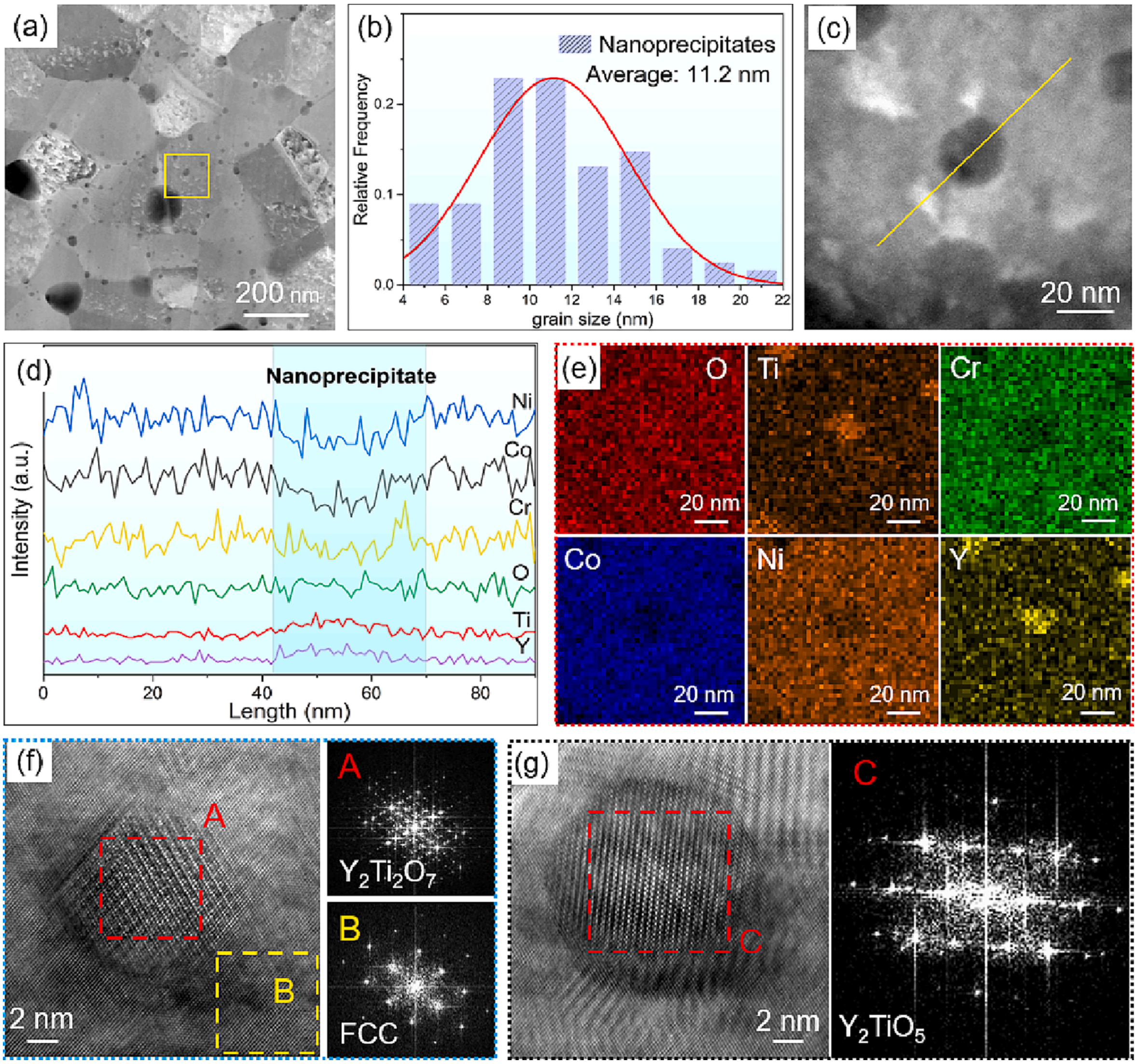

Fig. 6. Characterization of the nanoprecipitates in Y-ODS CoCrNi alloy. (a) HAADF-STEM image; (b) grain size distribution; (c) enlarged HAADF-STEM image from yellow square in (a); (d) EDX line scan profiles across a nanoprecipitate along with yellow line in (c); (e) corresponding EDX elemental maps; (f) high-resolution TEM image of $Y_2Ti_2O_7$ nanoprecipitate (A) and its surrounding fcc matrix (B) with their corresponding FFT patterns; (g) high-resolution TEM image of the Y_2TiO_5 nanoprecipitate (C) with its corresponding FFT pattern. The data of (c-e) are selected from a $Y_2Ti_2O_7$ nanoprecipitate. (For interpretation of the references to colour in this figure legend, the reader is referred to the web version of this article.)

4.1.1. *Solid solution strengthening*

The atomic radii of the Ti and Y are much larger compared with the constituent elements of Co, Cr, and Ni, especially for the atom Y, which is close to 50% larger than that of atom Ni. Thus, the effect of solid solution strengthening can be strong. However, the low content of the two elements greatly weakens the solid solution strengthening effect. The specific degree of strengthening can be expressed as the following equation [49]:

$$\Delta\sigma_{SS} = AG\varepsilon_S^{\frac{4}{3}}C^{\frac{2}{3}} \tag{2}$$

where $A = 0.1$ is a dimensionless material constant, G is the shear modulus of CoCrNi alloy (87 GPa [40]) and ε_S is the lattice strain caused by the difference in atomic radii between the solute and solvent. C is atomic concentration of the solute atoms. The effects of solid solution strengthening for Y and Ti were calculated to be 34 MPa and 25 MPa, respectively. Hence, $\Delta\sigma_{SS}$ of Y-ODS and Y_2O_3-ODS alloys were 59 MPa and 25 MPa, respectively.

4.1.2. *Grain boundary strengthening*

Grain boundary strengthening greatly depends on the average grain size (d) of fcc matrix. It can be calculated by the classical Hall-Petch relationship [48]:

$\Delta\sigma_{GB} = K^{HP}d^{-1/2}$ (3)

where K^{HP} is coefficient of Hall-Petch, varying with materials. Because both Y-ODS and Y_2O_3-ODS alloys were developed on the basis of CoCrNi, the $K^{HP} = 265$ MPa·μm$^{1/2}$ was chosen in this work [47]. Therefore, the strength increments originate from grain boundaries ($\Delta\sigma_{GB}$) of Y-ODS and Y_2O_3-ODS alloys are 499 MPa and 427 MPa, respectively.

4.1.3. *Twin boundary strengthening*

Similar to grain boundaries, twin boundaries also have a strengthening effect via impeding the movement of dislocations. The contribution from twin boundaries to enhance the yield strength, $\Delta\sigma_{TB}$, obeys the Hall-Petch type strengthening as well [50–52]:

$$\Delta\sigma_{TB} = V_{fT}K^{TB}\lambda_{TB}^{-\frac{1}{2}} \tag{4}$$

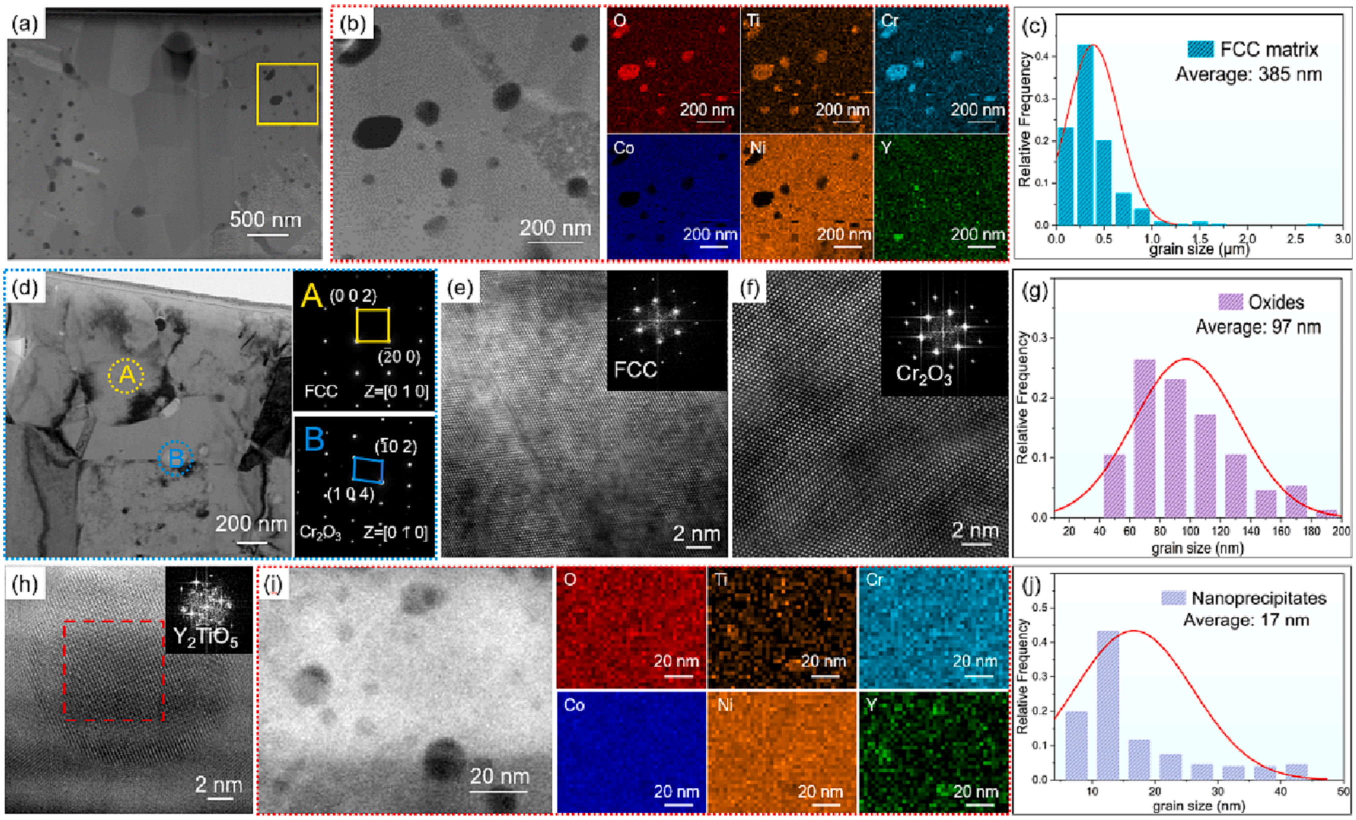

Fig. 7. Microstructure of the bulk Y_2O_3-ODS CoCrNi alloy. (a) HAADF-STEM image; (b) enlarged HAADF-STEM image from yellow square in (a) and corresponding STEM-EDX elemental maps; (c) grain size distribution of fcc matrix; (d) bright-field TEM image with selected SAED patterns of an fcc matrix grain (A) and an oxide particle (B), respectively; (e) high-resolution TEM image of fcc matrix; (f) high-resolution TEM image of the Cr_2O_3 oxide; (g) grain size distribution of Cr_2O_3 oxides; (h) high-resolution TEM image of the Y_2TiO_5 nanoprecipitate; (i) a representative HAADF-STEM image with its corresponding EDX elemental maps; and (j) grain size distribution of the Y_2TiO_5 nanoprecipitates. (For interpretation of the references to colour in this figure legend, the reader is referred to the web version of this article.)

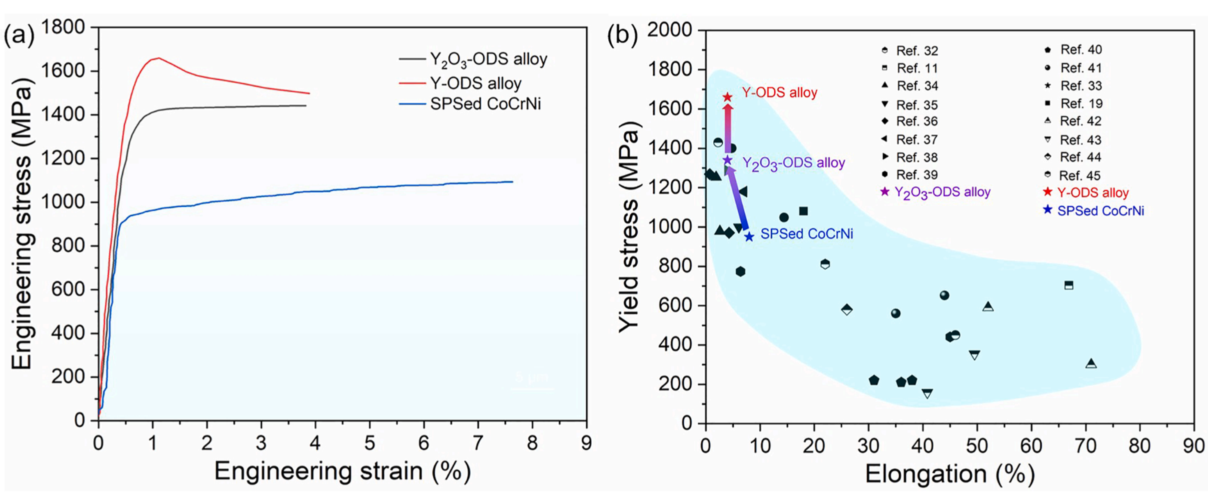

Fig. 8. Mechanical properties of the SPSed, Y-ODS, and Y_2O_3-ODS CoCrNi alloys. (a) Tensile engineering stress–strain curves; and (b) a comparison of tensile yield strength/elongation to failure of the present alloys with others.

where K^{TB} is a constant coefficient, approximately identical to K^{HP}, V_{fT} is the volume fraction of twins, and λ_{TB} is the average twin boundaries spacing (twin thickness). The calculated $\Delta\sigma_{TB}$ for Y-ODS and Y_2O_3-ODS alloy are 40 MPa and 44 MPa, respectively.

4.1.4. Precipitation strengthening

A high number density of oxides and nanoprecipitates will greatly strengthen the alloy by pinning dislocations during plastic deformation. The strengthening mechanisms mainly contain the Orowan dislocation bypass mechanism and the dislocation shearing particle mechanism, depending on the size, coherency with matrix, and the strength of the particles. The dislocation shearing mechanism is preferred when the particles are small, soft, and coherent with matrix, and otherwise, the Orowan dislocation bypass mechanism dominates. The $(Cr_{0.75}Ti_{0.25})_2O_3$

oxides in both alloys have an average size of ~100 nm and are incoherent with fcc matrix. Hence, the Orowan dislocation bypass mechanism plays a key role when dislocations move to the oxides. The increment in yield strength caused by $(Cr_{0.75}Ti_{0.25})_2O_3$ oxides can be calculated as follows [53]:

$$\sigma_{Or} = (0.538 \bullet \frac{Gbf_o^{0.5}}{D})\ln(\frac{D}{2b}) \tag{5}$$

where f_o is the volume fraction of Cr_2O_3 oxides and $b = \sqrt{2}/2a$ is the magnitude of Burgers vector ($a = 0.3569$ nm, the lattice parameter of the fcc matrix). $D = \sqrt{3/2}D_0$ is the real spatial diameter of $(Cr_{0.75}Ti_{0.25})_2O_3$ oxides (D_0 is the average size of the $(Cr_{0.75}Ti_{0.25})_2O_3$ oxides). The calculated incremental contribution to yield strength from the strengthening of $(Cr_{0.75}Ti_{0.25})_2O_3$ oxides $\Delta\sigma_O$ is ~85 MPa for Y-ODS and ~94 MPa for Y_2O_3-ODS alloy, respectively.

Considering the nanoprecipitates have two distinct structures in Y-ODS alloy, the coherent $Y_2Ti_2O_7$ pyrochlore structure and the incoherent Y_2TiO_5 orthorhombic structure, the strengthening mechanisms contributed by nanoprecipitates should be counted separately. Because it is technically challenging to determine the specific proportion of the two structures, the contribution of precipitation strengthening, $\Delta\sigma_P$, will be discussed as following: (1) assuming that all nanoprecipitates are incoherent with matrix, the strength increment of nanoprecipitates in Y-ODS alloy, $\Delta\sigma_{P1}$, can be obtained by Eq. (5) and the $\Delta\sigma_{P1}$ was calculated to be ~669 MPa; (2) assuming that all nanoprecipitates are coherent with matrix, the precipitation strengthening originates from coherent nanoprecipitates will follow the dislocation shearing mechanism. For dislocation shearing mechanism, the increment of strengthening can be ascribed to coherency strengthening ($\Delta\sigma_{cs}$), modulus mismatch strengthening ($\Delta\sigma_{ms}$) and order strengthening ($\Delta\sigma_{os}$) [54]. Prior to shearing the nanoprecipitates, the former two strengthening mechanisms occur. When the dislocations start to shear the nanoprecipitates, the strengthening will shift to the latter one. Therefore, $\Delta\sigma_P$ can be attributed to the larger of $\Delta\sigma_{cs} + \Delta\sigma_{ms}$ or $\Delta\sigma_{os}$. The values of $\Delta\sigma_{cs}$, $\Delta\sigma_{ms}$, and $\Delta\sigma_{os}$ can be obtained from Eqs. (6)-(8), respectively [54]:

$$\Delta\sigma_{cs} = M\alpha_\varepsilon(G\varepsilon_c)^{\frac{3}{2}}(\frac{rf_p}{0.5Gb})^{\frac{1}{2}} \tag{6}$$

$$\Delta\sigma_{ms} = M \bullet 0.0055 \bullet (\Delta G)^{\frac{3}{2}}(\frac{2f_p}{G})^{\frac{1}{2}}(\frac{r}{b})^{\frac{3m}{2}-1} \tag{7}$$

$$\Delta\sigma_{os} = M \bullet 0.81 \bullet \frac{\gamma_{apb}}{2b}(\frac{3\pi f_p}{8})^{\frac{1}{2}} \tag{8}$$

where $M = 3.06$ is Taylor factor, the average orientation factor for fcc structure, $\alpha_\varepsilon = 2.6$ is a constant for fcc metals, ε_c is the constrained lattice misfit between the matrix and nanoprecipitates, defined as $\varepsilon_c \approx \frac{2}{3} \bullet \frac{\Delta a}{a}$ (a is the lattice parameter of fcc matrix and Δa presents the lattice mismatch between them), r is the radius of nanoprecipitates, f_p represents the volume fraction of nanoprecipitates, ΔG is the shear modulus difference between the fcc matrix and nanoprecipitates (the shear modulus of $Y_2Ti_2O_7$ is 104 GPa [55]), $m = 0.85$, and γ_{apb} is the antiphase boundary energy (taking an intermediate value of 200 mJ/m^2 reported in literature [56]). The $\Delta\sigma_{cs}$, $\Delta\sigma_{ms}$, and $\Delta\sigma_{os}$ are determined to be 887, 119, and 250 MPa, respectively. Because $\Delta\sigma_{cs} + \Delta\sigma_{ms} > \Delta\sigma_{os}$, the strength contributions from coherent nanoprecipitates are coherency strengthening and modulus mismatch strengthening. Therefore, the $\Delta\sigma_{P2}$ of Y-ODS alloy reaches 1006 MPa. Obviously, the coherent nanoprecipitates play a significant role in enhancing the yield strength of Y-ODS alloy. Due to the existence of both coherent and incoherent nanoprecipitates, the $\Delta\sigma_P$ lies in the range of $\Delta\sigma_{P1}$ and $\Delta\sigma_{P2}$. Considering the uncertain proportion of these two types of nanoprecipitates, it is reasonable to take the average of $\Delta\sigma_{P1}$ and $\Delta\sigma_{P2}$ as $\Delta\sigma_P$, which is 838 MPa. As for Y_2O_3-ODS alloy, there is no coherent nanoprecipitates. Hence, $\Delta\sigma_P$ of Y_2O_3-ODS alloy by incoherency strengthening from Y_2TiO_5 nanoprecipitates follows Eq. (5) and was calculated to be ~562 MPa.

4.1.5. Dislocation strengthening

Dislocations can interact with each other and then hinder their motion, leading to strength enhancement. Thus, a high dislocation density will distinctly increase the yield strength of the alloy. The Bailey-Hirsch relationship [57] can be used to identify the increment of strength originating from dislocations:

$$\Delta\sigma_{Dis} = M\alpha Gb\rho^{\frac{1}{2}} \tag{9}$$

where $\alpha = 0.2$ for fcc structure and ρ is the dislocation density, which can be derived from the following equation [58]:

$$\rho = \frac{2\sqrt{3}\varepsilon}{db} \tag{10}$$

where ε is the microstrain of the alloy, obtained from Williamson-Hall method [59]:

$$\beta cos\theta_B = \frac{K\lambda}{d} + 4\varepsilon sin\theta_B \tag{11}$$

where β is the true XRD peak broadening and θ_B is the Bragg angle. $K = 0.9$ is a constant and $\lambda = 0.154$ nm represents the wavelength of Cu Kα radiation. The ε can be obtained by the slope of the $\beta cos\theta_B - 4sin\theta_B$ plot after fitting linearly [60]. According to the above equations, the ε, ρ, and $\Delta\sigma_{Dis}$ are calculated as 0.002, 9.7×10^{13} m^{-2}, and 131 MPa for Y-ODS alloy, and 0.0018, 6.4×10^{13} m^{-2}, and 108 MPa for Y_2O_3-ODS alloy, respectively.

4.1.6. Estimated overall strength

As mentioned above, all the strengthening contributions to yield strength of Y-ODS alloy and Y_2O_3-ODS alloy were calculated separately. Therefore, from the Eq. (1), the overall calculated yield strength of the alloys can be obtained as 1870 MPa and 1463 MPa, respectively. Note that the calculated overall strength is slightly larger than the experimental ones. The changes in concentration after the solute elements participating in oxidation and the possible differences in precipitation strengthening originated from nanoprecipitates with different sizes were neglected for simplicity. Precipitation strengthening is also simplified due to the indistinct concentration of those two nanoprecipitates in Y-ODS alloy. In addition, it is impossible to obtain samples with full density during the SPS consolidation and the presence of pores and defects in the sintered bulk alloys was not considered in the calculation of yield strength. The coalescence of these pores and defects will produce cracks and these cracks can propagate during tensile tests, leading to premature yield. Overall, the above analysis suggests that the dominant strengthening mechanisms in these two alloys are nanoprecipitate strengthening and grain boundary strengthening. The incremental strength originating from the two mechanisms is over one gigapascal, more than two thirds of the total calculated yield strength. To identify the reason for the superior yield strength of Y-ODS alloy compared with Y_2O_3-ODS alloy, the differences of the contributions from each strengthening mechanism between the two alloys were compared and further analyzed, as shown in Fig. 9. The main differences lie in the nanoprecipitate strengthening, the grain boundary strengthening, and the solid solution strengthening. Especially for the nanoprecipitate strengthening, the strength increment of Y-ODS CoCrNi is 276 MPa larger than that of Y_2O_3-ODS one.

4.2. The reason for superior yield strength of Y-ODS alloy

Based on the aforementioned analysis, the Y-ODS CoCrNi alloy via in situ oxidation shows much higher yield strength in comparison with Y_2O_3-ODS one via non-in-situ oxidation. The primary strengthening

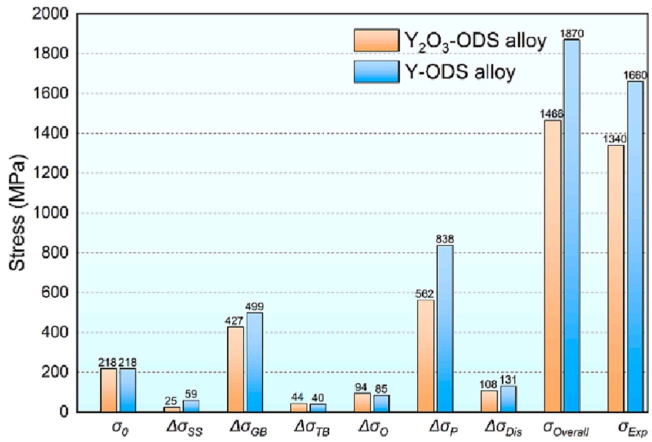

Fig. 9. Strengthening contributions of the yield strength in Y-ODS and Y_2O_3-ODS CoCrNi alloys.

mechanisms lie in nanoprecipitate strengthening, grain boundary strengthening, and solid solution strengthening. In order to uncover the nature of the nanoprecipitates, APT was used to quantitatively analyze the elemental partitioning at the atomic scale of Y-ODS CoCrNi alloy (Fig. 10). The reconstructed 3D atom maps show that the Co, Cr, and Ni are uniformly distributed in the fcc matrix, while the nanoprecipitates are rich in Y, Ti, and O. In addition, the typical atom map of Y in the fcc matrix (Fig. 10a) confirms that partial Y atoms were dissolved into the matrix. Quantitative analysis reveals that the dissolved Y atoms account for 32% of the total input Y atoms. This means that the remaining 68% of the Y atoms participate in oxidation, forming the nanoprecipitates. The significantly larger atomic radius of Y than that of Co, Cr, and Ni can explain why the solid solution strengthening of Y-ODS alloy is higher than Y_2O_3-ODS.

From the analysis of strengthening mechanism, the strength increment originating from nanoprecipitates made the largest contribution to the overall yield strength and the distinct strength increment difference of the two alloys lies in the strengthening of nanoprecipitates. One reason is that the nanoprecipitates formed in Y-ODS alloy are finer and more dispersed than those in Y_2O_3-ODS alloy. Based on the mechanism of oxides dispersion strengthening, the fine and uniform oxide particles can exert strong strengthening effect on the increase of yield strength. More significantly, the coherency strengthening of coherent $Y_2Ti_2O_7$ is higher than the Orowan strengthening of Y_2TiO_5 incoherent with fcc matrix, which is different from the coherent nanoprecipitates reported in other literatures [61–63]. In those works, the coherent nanoprecipitates exhibited relatively small strengthening. This should be due to that the $Y_2Ti_2O_7$ precipitates has high strength and hardness compared with those $L1_2$ phase or $D0_{22}$ phase. Thus, shearing the $Y_2Ti_2O_7$ precipitates requires a larger stress, resulting in a higher coherency strengthening.

Nanometric clusters were formed at the stage of mechanical alloying, containing Y, O and Ti elements (Fig. 3). The clusters started growing during SPS, and then their volume fraction increased with the increasing temperature. Then, the stoichiometry and structure of the nano-oxides stabilized with the first formation of pyrochlore $Y_2Ti_2O_7$ phase between 800 °C and 960 °C [64]. The nano-oxides gradually transformed from $Y_2Ti_2O_7$ to Y_2TiO_5 at 1100 °C with the holding time, which has been confirmed by Spartacus et al. [29] and Kim et al. [64]. However, the type of nanoprecipitates was also strongly influenced by the degree of oxygen contamination during ball milling [65]. An increase of oxygen concentration in the reactants would promote the formation of orthorhombic Y_2TiO_5 phases rather than the pyrochlore $Y_2Ti_2O_7$ phases. For the Y_2O_3-ODS alloy via non-in-situ oxidation, direct input of Y_2O_3 increased the oxygen concentration and thereby, induced the formation of orthorhombic Y_2TiO_5 phases but without the presence of pyrochlore $Y_2Ti_2O_7$ phase. Besides, the $(Cr_{0.75}Ti_{0.25})_2O_3$ oxide was formed in both alloys. Due to its high chemical affinity for O, the Cr element was usually oxidized during mechanical alloying [66]. In addition, the content of oxygen in the system is too high to be compensated by the addition of Y and Ti, resulting in the formation of Cr-Ti oxides. Adding sufficient amounts of Y and Ti to form the more stable oxides, such as $Y_2Ti_2O_7$ and Y_2TiO_5, which may further improve the mechanical properties of the Y-

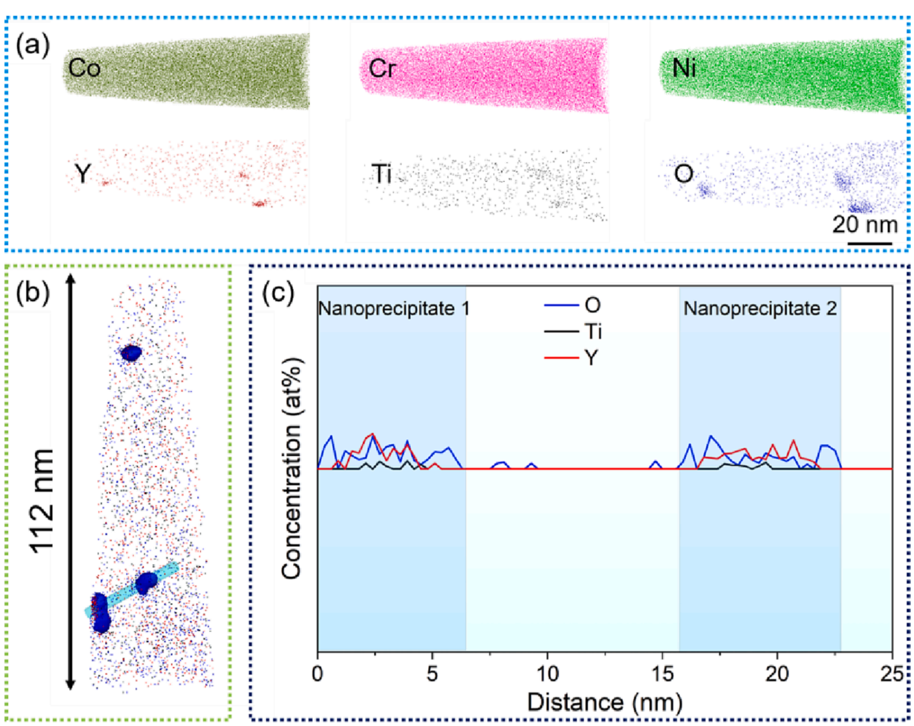

Fig. 10. 3D APT reconstruction of the Y-ODS CoCrNi alloy. (a) Co, Cr, Ni, Y, Ti and O atom maps in a typical APT tip; (b) 0.015 at.% (Y + O) *iso*-concentration surface showing the nanoprecipitates; (c) proximity histogram of concentration profiles.

ODS CoCrNi alloy.

5. Conclusions

In the present work, two types of ODS-CoCrNi alloys via in situ oxidation and non-in-situ oxidation were fabricated by mechanical alloying and SPS. The in-situ oxidation formation mechanism and its effect on microstructure and mechanical properties were characterized in detail. The strengthening contributions were analyzed. The main findings are summarized as follows:

(1) Both Y-ODS and Y_2O_3-ODS CoCrNi alloys consist of $(Cr_{0.75}Ti_{0.25})_2O_3$ oxides and Y-Ti-O nanoprecipitates dispersed in the fcc matrix. In Y-ODS CoCrNi alloy, ∼ 32% Y atoms were dissolved into the fcc matrix while the other Y participated in oxidation. Both fully coherent pyrochlore $Y_2Ti_2O_7$ and incoherent orthorhombic Y_2TiO_5 nanoprecipitates were formed in Y-ODS CoCrNi alloy, but only incoherent Y_2TiO_5 was detected in Y_2O_3-ODS one.

(2) The Y-ODS CoCrNi alloy shows an ultrahigh yield strength of 1660 MPa, which is 320 MPa higher than the Y_2O_3-ODS one, while maintains the same ductility. The dominant strengthening mechanisms are nanoprecipitate strengthening and grain boundary strengthening, taking more than two thirds of the total calculated yield strength. The higher strength of Y-ODS CoCrNi alloy is attributed to the ultrafine-grained fcc matrix and the presence of coherent $Y_2Ti_2O_7$ nanoprecipitates.

Declaration of Competing Interest

The authors declare that they have no known competing financial interests or personal relationships that could have appeared to influence the work reported in this paper.

Data availability

Data will be made available on request.

Acknowledgments

This work was financially supported by the National Natural Science Foundation of China (Grant No. 52122102) and Guangdong Innovative & Entrepreneurial Research Team Program (Grant No. 2016ZT06C279). APT research was conducted at the Inter-University 3D APT Unit of City University of Hong Kong (CityU), which is supported by the CityU grant 9360161. The authors also thank the Microscope and Imaging Center at Southern University of Science and Technology, China.

Appendix A. Supplementary data

XRD patterns of the powders for Y_2O_3-ODS alloy after different ball milling times were provided in Supplementary Fig. S1. Supplementary data to this article can be found online at https://doi.org/10.1016/j.matdes.2023.112141.

References

[1] B. Gludovatz, A. Hohenwarter, K.V.S. Thurston, H. Bei, Z. Wu, E.P. George, R. O. Ritchie, Exceptional damage-tolerance of a medium-entropy alloy CrCoNi at cryogenic temperatures, Nat. Commun. 7 (2016) 10602.
[2] E.P. George, W.A. Curtin, C.C. Tasan, High entropy alloys: A focused review of mechanical properties and deformation mechanisms, Acta Mater. 188 (2020) 435–474.
[3] Z. Zhang, H. Sheng, Z. Wang, B. Gludovatz, Z. Zhang, E.P. George, Q. Yu, S.X. Mao, R.O. Ritchie, Dislocation mechanisms and 3D twin architectures generate exceptional strength-ductility-toughness combination in CrCoNi medium-entropy alloy, Nat. Commun. 8 (2017) 14390.
[4] Z.J. Gu, Y.Z. Tian, W. Xu, S. Lu, X.L. Shang, J.W. Wang, G.W. Qin, Optimizing transformation-induced plasticity in CoCrNi alloys by combined grain refinement and chemical tuning, Scripta Mater. 214 (2022), 114658.
[5] J. Miao, C.E. Slone, T.M. Smith, C. Niu, H. Bei, M. Ghazisaeidi, G.M. Pharr, M. J. Mills, The evolution of the deformation substructure in a Ni-Co-Cr equiatomic solid solution alloy, Acta Mater. 132 (2017) 35–48.
[6] Y.L. Zhao, T. Yang, Y. Tong, J. Wang, J.H. Luan, Z.B. Jiao, D. Chen, Y. Yang, A. Hu, C.T. Liu, J.J. Kai, Heterogeneous precipitation behavior and stacking-fault-mediated deformation in a CoCrNi-based medium-entropy alloy, Acta Mater. 138 (2017) 72–82.
[7] N. An, Y. Sun, Y. Wu, J. Tian, Z. Li, Q. Li, J. Chen, X. Hui, High temperature strengthening via nanoscale precipitation in wrought CoCrNi-based medium-entropy alloys, Mater. Sci. Eng. A 798 (2020), 140213.
[8] P. Sathiyamoorthi, J. Moon, J.W. Bae, P. Asghari-Rad, H.S. Kim, Superior cryogenic tensile properties of ultrafine-grained CoCrNi medium-entropy alloy produced by high-pressure torsion and annealing, Scripta Mater. 163 (2019) 152–156.
[9] S. Praveen, J.W. Bae, P. Asghari-Rad, J.M. Park, H.S. Kim, Ultra-high tensile strength nanocrystalline CoCrNi equi-atomic medium entropy alloy processed by high-pressure torsion, Mater. Sci. Eng. A 735 (2018) 394–397.
[10] I. Moravcik, V. Hornik, P. Minárik, L. Li, I. Dlouhy, M. Janovska, D. Raabe, Z. Li, Interstitial doping enhances the strength-ductility synergy in a CoCrNi medium entropy alloy, Mater. Sci. Eng. A 781 (2020), 139242.
[11] I. Moravcik, H. Hadraba, L. Li, I. Dlouhy, D. Raabe, Z. Li, Yield strength increase of a CoCrNi medium entropy alloy by interstitial nitrogen doping at maintained ductility, Scripta Mater. 178 (2020) 391–397.
[12] X.H. Du, W.P. Li, H.T. Chang, T. Yang, G.S. Duan, B.L. Wu, J.C. Huang, F.R. Chen, C.T. Liu, W.S. Chuang, Y. Lu, M.L. Sui, E.W. Huang, Dual heterogeneous structures lead to ultrahigh strength and uniform ductility in a Co-Cr-Ni medium-entropy alloy, Nat. Commun. 11 (2020) 2390.
[13] L. Yang, D. Liang, Z. Cheng, R. Duan, C. Zhong, J. Luan, Z. Jiao, F. Ren, Simultaneous enhancement of strength and ductility via microband formation and nanotwinning in an $L1_2$-strengthened alloy, Fundam. Res. (2022).
[14] L. Zhang, S. Ukai, T. Hoshino, S. Hayashi, X. Qu, Y_2O_3 evolution and dispersion refinement in Co-base ODS alloys, Acta Mater. 57 (12) (2009) 3671–3682.
[15] L. Yang, C. Zhao, W. Zhu, Z. Cheng, P. Wei, F. Ren, Microstructure, mechanical properties, and sliding wear behavior of oxide-dispersion-strengthened FeMnNi alloy fabricated by spark plasma sintering, Metall. Mater. Trans. A 51 (6) (2020) 2796–2810.
[16] T.M. Smith, C.A. Kantzos, N.A. Zarkevich, B.J. Harder, M. Heczko, P.R. Gradl, A. C. Thompson, M.J. Mills, T.P. Gabb, J.W. Lawson, A 3D printable alloy designed for extreme environments, Nature 617 (7961) (2023) 513–518.
[17] C. Lu, M. Li, P. Xiu, X. Wang, G. Velişa, L. Jiang, K.L. More, J.D. Poplawsky, Y. Chang, Y. Zhang, L. Wang, High radiation tolerance of an ultrastrong nanostructured NiCoCr alloy with stable dispersed nanooxides and fine grain structure, J. Nucl. Mater. 557 (2021), 153316.
[18] Z. Cheng, L. Yang, W. Mao, Z. Huang, D. Liang, B. He, F. Ren, Achieving high strength and high ductility in a high-entropy alloy by a combination of a heterogeneous grain structure and oxide-dispersion strengthening, Mater. Sci. Eng. A 805 (2021), 140544.
[19] J.B. Seol, D. Haley, D.T. Hoelzer, J.H. Kim, Influences of interstitial and extrusion temperature on grain boundary segregation, Y-Ti-O nanofeatures, and mechanical properties of ferritic steels, Acta Mater. 153 (2018) 71–85.
[20] X. Mao, K.H. Oh, S.H. Kang, T.K. Kim, J. Jang, On the coherency of $Y_2Ti_2O_7$ particles with austenitic matrix of oxide dispersion strengthened steel, Acta Mater. 89 (2015) 141–152.
[21] M.P. Phaniraj, D.-I. Kim, J.-H. Shim, Y.W. Cho, Microstructure development in mechanically alloyed yttria dispersed austenitic steels, Acta Mater. 57 (6) (2009) 1856–1864.
[22] G.R. Odette, M.J. Alinger, B.D. Wirth, Recent Developments in Irradiation-Resistant Steels, Annu. Rev. Mater. Sci. 38 (1) (2008) 471–503.
[23] S. Ukai, M. Fujiwara, Perspective of ODS alloys application in nuclear environments, J. Nucl. Mater. 307–311 (2002) 749–757.
[24] Y. Wu, E.M. Haney, N.J. Cunningham, G.R. Odette, Transmission electron microscopy characterization of the nanofeatures in nanostructured ferritic alloy MA957, Acta Mater. 60 (8) (2012) 3456–3468.
[25] S.Y. Zhong, J. Ribis, V. Klosek, Y. de Carlan, N. Lochet, V. Ji, M.H. Mathon, Study of the thermal stability of nanoparticle distributions in an oxide dispersion strengthened (ODS) ferritic alloys, J. Nucl. Mater. 428 (1-3) (2012) 154–159.
[26] H. Kishimoto, M.J. Alinger, G.R. Odette, T. Yamamoto, TEM examination of microstructural evolution during processing of 14CrYWTi nanostructured ferritic alloys, J. Nucl. Mater. 329–333 (2004) 369–371.
[27] R. Chinnappan, Thermodynamic stability of oxide phases of Fe-Cr based ODS steels via quantum mechanical calculations, Calphad 45 (2014) 188–193.
[28] P. Unifantowicz, T. Płociński, C.A. Williams, R. Schäublin, N. Baluc, Structure of complex oxide nanoparticles in a Fe-14Cr-2W-0.3Ti-0.3Y_2O_3 ODS RAF steel, J. Nucl. Mater. 442 (1-3) (2013) S158–S163.
[29] G. Spartacus, J. Malaplate, F.D. Geuser, I. Mouton, D. Sornin, M. Perez, R. Guillou, B. Arnal, E. Rouesne, A. Deschamps, Chemical and structural evolution of nano-oxides from mechanical alloying to consolidated ferritic oxide dispersion strengthened steel, Acta Mater. 233 (2022), 117992.
[30] A. Hirata, T. Fujita, Y.R. Wen, J.H. Schneibel, C.T. Liu, M.W. Chen, Atomic structure of nanoclusters in oxide-dispersion-strengthened steels, Nat. Mater. 10 (12) (2011) 922–926.
[31] J. Ribis, Y.d. Carlan, Interfacial strained structure and orientation relationships of the nanosized oxide particles deduced from elasticity-driven morphology in oxide dispersion strengthened materials, Acta Mater. 60 (2012) 238–252.

[32] H. Huang, J. Wang, H. Yang, S. Ji, H. Yu, Z. Liu, Strengthening CoCrNi medium-entropy alloy by tuning lattice defects, Scripta Mater. 188 (2020) 216–221.

[33] I. Moravcik, L. Gouvea, V. Hornik, Z. Kovacova, M. Kitzmantel, E. Neubauer, I. Dlouhy, Synergic strengthening by oxide and coherent precipitate dispersions in high-entropy alloy prepared by powder metallurgy, Scripta Mater. 157 (2018) 24–29.

[34] M. Li, Y. Guo, H. Wang, J. Shan, Y. Chang, Microstructures and mechanical properties of oxide dispersion strengthened CoCrFeNi high-entropy alloy produced by mechanical alloying and spark plasma sintering, Intermetallics 123 (2020), 106819.

[35] X. Liu, H. Yin, Y. Xu, Microstructure, mechanical and tribological properties of oxide dispersion strengthened high-entropy alloys, Materials (Basel) 10 (2017) 1312.

[36] H. Hadraba, Z. Chlup, A. Dlouhy, F. Dobes, P. Roupcova, M. Vilemova, J. Matejicek, Oxide dispersion strengthened CoCrFeNiMn high-entropy alloy, Mater. Sci. Eng. A 689 (2017) 252–256.

[37] J.Y. He, W.H. Liu, H. Wang, Y. Wu, X.J. Liu, T.G. Nieh, Z.P. Lu, Effects of Al addition on structural evolution and tensile properties of the FeCoNiCrMn high-entropy alloy system, Acta Mater. 62 (2014) 105–113.

[38] I. Moravcik, J. Cizek, J. Zapletal, Z. Kovacova, J. Vesely, P. Minarik, M. Kitzmantel, E. Neubauer, I. Dlouhy, Microstructure and mechanical properties of $Ni_{1,5}Co_{1,5}CrFeTi_{0,5}$ high entropy alloy fabricated by mechanical alloying and spark plasma sintering, Mater. Des. 119 (2017) 141–150.

[39] X. Jin, J. Bi, L. Zhang, Y. Zhou, X. Du, Y. Liang, B. Li, A new $CrFeNi_2Al$ eutectic high entropy alloy system with excellent mechanical properties, J. Alloy. Compd. 770 (2019) 655–661.

[40] Z. Wu, H. Bei, G.M. Pharr, E.P. George, Temperature dependence of the mechanical properties of equiatomic solid solution alloys with face-centered cubic crystal structures, Acta Mater. 81 (2014) 428–441.

[41] R. Chang, W. Fang, H. Yu, X. Bai, X. Zhang, B. Liu, F. Yin, Heterogeneous banded precipitation of $(CoCrNi)_{93}Mo_7$ medium entropy alloys towards strength–ductility synergy utilizing compositional inhomogeneity, Scripta Mater. 172 (2019) 144–148.

[42] H.W. Deng, M.M. Wang, Z.M. Xie, T. Zhang, X.P. Wang, Q.F. Fang, Y. Xiong, Enhancement of strength and ductility in non-equiatomic CoCrNi medium-entropy alloy at room temperature via transformation-induced plasticity, Mater. Sci. Eng. A 804 (2021), 140516.

[43] Z. Wang, I. Baker, Z. Cai, S. Chen, J.D. Poplawsky, W. Guo, The effect of interstitial carbon on the mechanical properties and dislocation substructure evolution in $Fe_{40.4}Ni_{11.3}Mn_{34.8}Al_{7.5}Cr_6$ high entropy alloys, Acta Mater. 120 (2016) 228–239.

[44] Z. Wang, I. Baker, W. Guo, J.D. Poplawsky, The effect of carbon on the microstructures, mechanical properties, and deformation mechanisms of thermo-mechanically treated $Fe_{40.4}Ni_{11.3}Mn_{34.8}Al_{7.5}Cr_6$ high entropy alloys, Acta Mater. 126 (2017) 346–360.

[45] Y.L. Zhao, T. Yang, J.H. Zhu, D. Chen, Y. Yang, A. Hu, C.T. Liu, J.J. Kai, Development of high-strength Co-free high-entropy alloys hardened by nanosized precipitates, Scripta Mater. 148 (2018) 51–55.

[46] S. Pan, C. Zhao, P. Wei, F. Ren, Sliding wear of CoCrNi medium-entropy alloy at elevated temperatures: Wear mechanism transition and subsurface microstructure evolution, Wear 440–441 (2019), 203108.

[47] S. Yoshida, T. Bhattacharjee, Y. Bai, N. Tsuji, Friction stress and Hall-Petch relationship in CoCrNi equi-atomic medium entropy alloy processed by severe plastic deformation and subsequent annealing, Scripta Mater. 134 (2017) 33–36.

[48] Z. Cheng, W. Zhu, L. Yang, C. Zhao, P. Wei, F. Ren, Tuning the mechanical properties of $Fe_x(CoMoNi)_{100-x}$ high-entropy alloys via controlled formation of hard μ phase, Mater. Sci. Eng. A 773 (2020), 138881.

[49] O.N. Senkov, J.M. Scott, S.V. Senkova, D.B. Miracle, C.F. Woodward, Microstructure and room temperature properties of a high-entropy TaNbHfZrTi alloy, J. Alloy. Compd. 509 (20) (2011) 6043–6048.

[50] X. Li, Y. Wei, L. Lu, K. Lu, H. Gao, Dislocation nucleation governed softening and maximum strength in nano-twinned metals, Nature 464 (7290) (2010) 877–880.

[51] Y.F. Shen, L. Lu, Q.H. Lu, Z.H. Jin, K. Lu, Tensile properties of copper with nano-scale twins, Scripta Mater. 52 (10) (2005) 989–994.

[52] X.H. Chen, L. Lu, K. Lu, Grain size dependence of tensile properties in ultrafine-grained Cu with nanoscale twins, Scripta Mater. 64 (4) (2011) 311–314.

[53] T. Gladman, Precipitation hardening in metals, Mater. Sci. Technol. 15 (1) (1999) 30–36.

[54] H. Wen, T.D. Topping, D. Isheim, D.N. Seidman, E.J. Lavernia, Strengthening mechanisms in a high-strength bulk nanostructured Cu–Zn–Al alloy processed via cryomilling and spark plasma sintering, Acta Mater. 61 (8) (2013) 2769–2782.

[55] L.F. He, J. Shirahata, T. Nakayama, T. Suzuki, H. Suematsu, I. Ihara, Y. Bao, T. Komatsu, K. Niihara, Mechanical properties of Y2Ti2O7, Scripta Mater. 64 (6) (2011) 548–551.

[56] R.W. Kozar, A. Suzuki, W.W. Milligan, J.J. Schirra, M.F. Savage, T.M. Pollock, Strengthening mechanisms in polycrystalline multimodal nickel-base superalloys, Metall. Mater. Trans. A 40 (7) (2009) 1588–1603.

[57] K. Ma, H. Wen, T. Hu, T.D. Topping, D. Isheim, D.N. Seidman, E.J. Lavernia, J. M. Schoenung, Mechanical behavior and strengthening mechanisms in ultrafine grain precipitation-strengthened aluminum alloy, Acta Mater. 62 (2014) 141–155.

[58] G.K. Williamson, R.E. Smallman, Dislocation densities in some annealed and cold-worked metals from measurements on the X-ray debye-scherrer spectrum, Philos. Mag. 1 (1956) 34–46.

[59] D. Qi, B. Fu, K. Du, T. Yao, C. Cui, J. Zhang, H. Ye, Temperature effects on the transition from Lomer-Cottrell locks to deformation twinning in a Ni-Co-based superalloy, Scripta Mater. 125 (2016) 24–28.

[60] J.Y. He, H. Wang, H.L. Huang, X.D. Xu, M.W. Chen, Y. Wu, X.J. Liu, T.G. Nieh, K. An, Z.P. Lu, A precipitation-hardened high-entropy alloy with outstanding tensile properties, Acta Mater. 102 (2016) 187–196.

[61] F. He, D. Chen, B. Han, Q. Wu, Z. Wang, S. Wei, D. Wei, J. Wang, C.T. Liu, J.J. Kai, Design of $D0_{22}$ superlattice with superior strengthening effect in high entropy alloys, Acta Mater. 167 (2019) 275–286.

[62] T. Xiong, S. Zheng, J. Pang, X. Ma, High-strength and high-ductility $AlCoCrFeNi_{2.1}$ eutectic high-entropy alloy achieved via precipitation strengthening in a heterogeneous structure, Scripta Mater. 186 (2020) 336–340.

[63] Y. Tong, D. Chen, B. Han, J. Wang, R. Feng, T. Yang, C. Zhao, Y.L. Zhao, W. Guo, Y. Shimizu, C.T. Liu, P.K. Liaw, K. Inoue, Y. Nagai, A. Hu, J.J. Kai, Outstanding tensile properties of a precipitation-strengthened $FeCoNiCrTi_{0.2}$ high-entropy alloy at room and cryogenic temperatures, Acta Mater. 165 (2019) 228–240.

[64] S.-W. Kim, T. Shobu, S. Ohtsuka, T. Kaito, M. Inoue, M. Ohnuma, Kinetic approach for growth and coalescence of nano-size oxide particles in 9Cr-ODS steel using high-energy synchrotron radiation X-rays in SPring-8, Mater. Trans. 50 (4) (2009) 917–921.

[65] M.A. Thual, J. Ribis, T. Baudin, V. Klosek, Y. de Carlan, M.H. Mathon, Relaxation path of nanoparticles in an oxygen-enriched ferritic oxide-dispersion-strengthened alloy, Scripta Mater. 136 (2017) 37–40.

[66] D. Liang, C. Zhao, W. Zhu, P. Wei, F. Jiang, Y. Zhang, Q. Sun, F. Ren, Overcoming the strength-ductility trade-off via the formation of nanoscale Cr-rich precipitates in an ultrafine-grained FCC CrFeNi medium entropy alloy matrix, Mater. Sci. Eng. A 762 (2019), 138107.